



Electrodeposition of nickel–iron on stainless steel as an efficient electrocatalyst coating for the oxygen evolution reaction in alkaline conditions

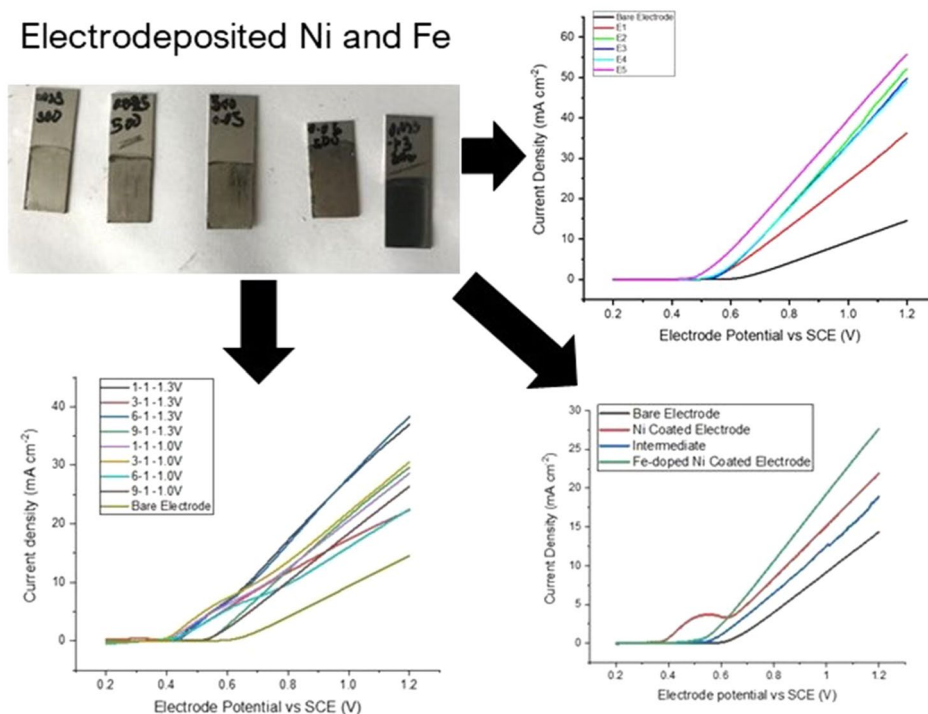
Yifu Wang¹ · Nigel Williamson² · Richard Dawson^{1,3} · Nuno Bimbo^{1,4}

Received: 5 August 2022 / Accepted: 17 November 2022 / Published online: 5 December 2022
© The Author(s) 2022

Abstract

Significant amount of effort has been devoted in the development of water electrolysis technology as the prime technology for green hydrogen production. In this paper, we investigate nickel–iron-based electrocatalytic coatings on stainless-steel substrates for commercial alkaline water electrolyzers. Stainless steel electrodes for water electrolysis have received attention lately, showing that they can be a low-cost substrate for water electrolysis. Coating stainless steel with low-cost electrocatalysts can prove beneficial to lower overpotential for the oxygen evolution reaction (OER), thereby reducing the overall energy consumption of water electrolysis at an affordable cost. We show that NiFe-deposited substrates have an overpotential of 514 mV at 10 mA cm⁻² current. The substrates also exhibited excellent stability in strong alkaline condition for 60 h under continuous 1.2 V working potential vs SCE. The results in full-cell electrolyzers demonstrate that the electrolyser with the NiFe-coated anode could generate nearly six times as much current density compared with the bare stainless-steel substrate.

Graphical abstract



Extended author information available on the last page of the article

Keywords Hydrogen · Alkaline electrolysis · Nickel–iron · Oxygen evolution reaction · Clean energy · Electrocatalyst

1 Introduction

Hydrogen could play an important role in a future decarbonised energy system. Compared to fossil fuels, hydrogen is a much cleaner and more environmentally friendly energy vector, presenting many advantages, including high energy density per unit mass and an emissions-free conversion of energy at point-of-use. However, apart from small concentrations in very specific circumstances such as gas or oil deposits, hydrogen cannot be found in pure state (as molecular hydrogen) on earth and is instead present associated to other compounds, such as in biomass or water. To obtain molecular hydrogen, specific processes such as coal gasification, steam reforming, and water electrolysis are required, which depend on the hydrogen source. Natural gas is currently the main source of hydrogen production in the world, accounting for around 95% of global hydrogen production in 2018 [1]. Natural gas (or methane, specifically) is treated in a process denominated steam methane reforming, which is energy intensive, requires a fossil fuel precursor and produces carbon dioxide. Water electrolysis only contributes a small fraction of global hydrogen production, but there are many advantages of electrolysis over conventional industrial hydrogen production processes. First, electrolysis can produce hydrogen as pure as 99.999% [2]. Second, if renewable energy sources such as wind and solar energy are used, electrolysis could achieve zero-carbon emissions. The International Energy Agency (IEA) predicts that the cost of hydrogen production by renewable energy sources will be reduced by 30% by 2030, owing to the scale up of hydrogen production and reduced cost of renewable energy [3].

At present, alkaline water electrolysis is a low-cost and mature hydrogen production technology which has been commercialised by industry. Current alkaline water electrolyzers can generate up to 1000 m³/h hydrogen, meaning they are capable of large-scale hydrogen production [4]. Alkaline water electrolysis is also attractive in terms of its investment cost, which is around 1000–1200 euros per kW [5]. In addition, alkaline water electrolyzers have longer lifetimes and lower maintenance costs compared to PEM electrolyzers [6], which are another type of commercial electrolysis system. However, there are many other limitations that place alkaline water electrolyzers in strong competition in hydrogen production markets compared with other alternatives, including low current densities, limited operational pressure and electrode corrosion.

Some care must be taken when selecting materials in alkaline electrolysis. For instance, the physical and chemical

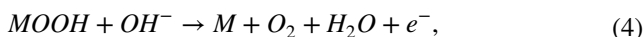
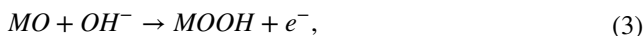
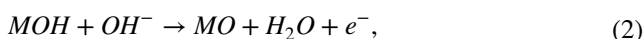
properties of current collectors could have significant impact on the charge transfer during electrolysis. Iron-based substrates are not suitable in alkaline water electrolysis due to their instability under anodic condition [7]. Some nickel-based substrates such as nickel foam have good stability under anodic condition and high electrolyte concentration [8], however they will add a lot of extra cost to the overall electrolyzers due to the high cost of nickel foam. Stainless steel is a good option as the electrode of alkaline water electrolyser due to several reasons. First, in terms of cost, stainless steel is a lower-cost material compared to Ni-based substrates. Second, the presence of chromium provides corrosion resistance due to the formation of a thin chromium oxide layer which passivates the stainless-steel electrode during operation. Lastly, due to the presence of nickel and iron, stainless steel has intrinsic electrocatalytic OER activity during operation with gradual formation of nickel- and iron-based OER-active species [9].

In addition to stability, another reason for using nickel-based substrates are its catalytic properties as nickel metal or nickel compounds are very promising electrocatalysts for both the oxygen evolution (OER) and the hydrogen evolution reaction (HER) [10]. Stainless steel 316 contains approximately 11% nickel [11], for which a noticeable improvement of electrolysis performance is expected compared to non-nickel-containing substrates. There are some successful experiences reported in the literature where researchers modified the stainless-steel electrodes by controlled surface oxidation of stainless steel, which could be used directly as electrodes in alkaline water electrolyzers with high current density and stability [12–15]. There are a few requirements that must be satisfied for industrial use of long-term electrolysis operations. First, substrates must have good electrical conductivity so that they can provide efficient electron transfer and high Coulombic efficiency; second, substrates must have high catalytic activity for both HER and OER, of which the reaction kinetics are a limiting factor in the overall energy consumption of electrolysis; last, substrates must have good corrosion resistance for long-term operation under harsh conditions, e.g. high electrolyte concentration and high anodic current density [13]. Stainless steel itself could not satisfy these requirements; therefore, an appropriate coating material is essential for stainless steel to be used as an alkaline water electrolyser substrate.

To improve the performance of alkaline water electrolyzers, many research papers have described the progress of electrocatalyst development for both OER and HER in acidic and alkaline conditions. This is the consequence of

the urgent need for low-cost, stable and highly active electrocatalysts for efficient hydrogen production. OER is considered the most difficult reaction, as it is more kinetically unfavourable than HER. As such, much current effort has focused on developing OER electrocatalysts.

A good understanding in reaction mechanisms and catalyst active sites is very important to guide the design the OER electrocatalysts. In alkaline water electrolysis, OER is the half-reaction that occurs at the anode. Different reaction mechanisms have been suggested, of which the most widely agreed mechanism is known as the conventional adsorbate evolution mechanism [16], which is described by Eqs. (1)–(4) [17].



where M represents metal centre of active site.

Ideally, the OER occurs with no additional free energy gap for each of the steps shown in Eq. 1–4, i.e. the free energy remains 1.23 eV. The overall overpotential of OER is limited by the rate-determining step, which is the one that has the highest ΔG . The change of ΔG is dependent on applied potential and pH; however, the overpotential is independent of these two parameters as it is assumed that the equilibrium potential also changes in the same manner as ΔG [18]. To design OER electrocatalysts, researchers chose $\Delta G_{O^*}^0 - \Delta G_{HO^*}^0$ as performance descriptor, which is usually illustrated in a volcano-shaped plot [19], 20. A good electrocatalyst is expected to be positioned on the peak or as close to the peak point as possible in volcano plot.

Research on improving electrolyser efficiency is mainly focused on reducing the overpotential for the OER, on which the optimum design and operation of the electrolyser relies. This means that anode material development plays a key role in improving overall electrolyser performance. It is accepted that precious metal-based catalyst such as RuO_2 and IrO_2 are the state-of-the-art materials for the OER, and they have reported overpotentials of 358 and 411 mV at a current density of 10 mA cm^{-2} for the OER in alkaline solution, respectively [21]. Despite the high OER activity, precious metal-based catalysts are not ideal candidates for industrial-scale application of alkaline electrolysis, due to their high prices and low abundance. Cheaper transition metal-based materials would be more popular choices due to their cost, but their susceptibility to corrosion has been a research challenge for decades [22]. Therefore, development and design of superior low-cost transition metal-based OER catalysts such as metal

oxides, hydroxides, and phosphides have attracted significant attention from researchers.

One of the main benchmarks to assess OER kinetics is overpotential at 10 mA cm^{-2} [23]. In addition to this, many other properties require consideration; for example, catalysts must have good stability in aggressive operating conditions such as high temperatures and high electrolyte concentrations. Electrocatalysts with poor stability will result in active site poisoning and electrode corrosion, thereby lowering the overall efficiency of electrolysis. Electrode stability is assessed in different ways by different researchers, with Zayat et al. suggesting that highly stable OER catalysts should show little performance deviation when operating under 1 A cm^{-2} for 1000 h [24]. In addition to overpotential and stability, the cost of raw materials should be low, so earth-abundant elements should be predominant, in order to satisfy commercial, environmental and sustainable criteria [25]. Furthermore, the electrocatalysts should have good compatibility and wettability in the electrolyte and must not dissolve [26].

Although Ru, Ir and Rh-based catalysts exhibit outstanding performance as electrocatalysts in electrolysis, their high cost, and poor stability preclude them to become best options for commercial electrolysers. As alternatives, non-noble metal-based materials such as transition metal oxides, hydroxides, chalcogenides and sulphides have been researched and reported as better anode materials for alkaline water electrolysis [27].

Coating electrocatalysts on cheap, robust substrates such as stainless steel has several advantages, since it can provide low-cost, stable and durable electrodes for the OER. However, it is important to bear in mind that catalyst performance is significantly dependent on the physical and chemical properties of these systems. For coatings, this includes quality and uniformity when they were deposited as a thin layer on substrates, for which the selection of coating technique plays a really important role when fabricating high-performance electrodes. There are a number of successful coating techniques reported in the literature for OER catalysts. For example, Dong et al. reported dip-coating of Ni-Fe-based OER electrocatalysts on nickel foams. The electrodes achieved 210 mV overpotential under a current density of 10 mA cm^{-2} in a 1 M KOH solution, and no significant degradation was observed at 50 h operation under 50 mA cm^{-2} [28]. Babar and Joya fabricated NiO_x nanoflakes by spray coating, which achieved 250 mV at 10 mA cm^{-2} [27]. This shows that coatings can improve reaction kinetics for the OER, and the goal is to develop methods to coat substrates that can be affordable, easily scalable and uniform, to enable large-scale manufacturing of low-cost electrolysers.

This paper reports the synthesis and testing of nickel-based electrocatalysts by electrodeposition and hydrothermal deposition on stainless-steel 316. The electrodes were

produced using different methods, including different pHs, concentrations and precursors, and their electrochemical performance was measured. This focussed mostly on overpotential at 10 mA cm^{-2} and stability under working conditions for 15 h. Results for a full-cell electrolyser are also shown, highlighting the large improvement obtained from Ni–Fe coatings over bare stainless-steel electrodes.

The deposited nickel-based materials on stainless steel undergo a few phase transformations, which were firstly explained by Bode 50 years ago [36]. The Bode diagram presents electrochemical pathways of α - and β -phases of nickel hydroxide, and β - and γ -phases of oxyhydroxide formation in KOH electrolyte. α -Ni(OH)₂ is an unstable phase which can be easily oxidised to β -Ni(OH)₂ irreversibly after ageing in alkaline solution (e.g. KOH). α -Ni(OH)₂ can be oxidised directly to form γ -NiOOH by applying an electrical potential. The redox reaction which transforms between α -Ni(OH)₂ and γ -NiOOH is a reversible reaction. When the α -Ni(OH)₂ is aged to β -Ni(OH)₂, it will be oxidised to β -NiOOH when an electrical potential is applied, during which process the oxidation states of Ni is increased from 2.0–2.2 to 2.7–3.0 [37]. Further oxidation of β -NiOOH will form γ -NiOOH via an irreversible oxidation reaction.

Some reports such as Meng et al. suggested that it is very challenging to synthesise α -Ni(OH)₂ by a direct reaction using Ni²⁺ salts [38] and the presence of this phase is difficult to identify experimentally. In addition, the literature is ambiguous on whether the β -phase is more OER active than the γ -phase. There is some debate on which of β -NiOOH or γ -NiOOH is responsible for enhanced OER. In general, it is believed that β -NiOOH is more active than γ -NiOOH [37]. However, Bediako et. al suggested that γ -NiOOH may be intrinsically more active toward the OER than β -NiOOH-active sites by the analogy of nickel-borate OER catalyst developed by Bediako et al. [39].

The role of Fe in the boost of OER activity in KOH electrolyte has been investigated. For example, Klaus et al. characterised Ni-based catalysts in both Fe-free and Fe-containing KOH and found that the electrodes aged in Fe-containing electrolyte exhibited much higher OER activity and lower overpotential compared with those aged in Fe-free electrolyte [40]. Despite the role of Fe having been studied, the conclusions found in the literature are still contradictory, and those conclusions are summarised by Anantharaj et al. who have comprehensively reviewed the literature that studied the magical role of Fe in alkaline electrolysis [41].

Spanos et al. also investigated the effect of iron impurities on transition metal catalysts include Ni-based oxides for OER in alkaline environment [42]. As concluded by many other research groups [41], they too found that the OER activity of Ni-based catalysts was improved by orders of magnitude when adding Fe impurities in electrolyte rather than Fe-free electrolyte or catalysts. This improvement could

be significant with trace amounts of Fe addition, whereas higher Fe addition would cause an adverse effect on OER activity of Ni-based catalysts. One of the biggest problems of single-step electrodeposition using Ni²⁺ and Fe^{2+/3+} solution is the effect of anomalous co-deposition, which means that one of the metals is deposited preferentially in the solution if it contains more than two species of metallic ions [43]. Consequently, and in the case of single-step electrodeposition, the coating will be composed of much higher Fe content than Ni. Given that Fe-based oxides are not as active as Ni-based oxides as OER catalysts [41], excessive amounts of Fe in NiFe system will weaken the overall electrochemical performance in alkaline solutions, due to fewer available active sites from Ni-based oxides. Separating Ni and Fe deposition could allow sufficient Ni growth as well as preventing excessive Fe deposition to maximise the activity of NiFe-based catalysts.

2 Materials and methods

Different preparation methods were followed for electrode fabrication. In the first set of experiments, the effect of pH, Ni²⁺:Fe²⁺ ratio and deposition time was investigated, trying to ascertain how these would influence the chemical properties and electrochemical performance of electrodes. The electrodeposition was carried out in an electrolyte that contained nickel and iron sulfate. The second set of experiments was designed to investigate the effect of using alternative metal salts (nickel nitrate and iron nitrate) on the coating material characterisation and electrode performance. Finally, the last set of experiments was done using multistep electrodeposition and thermal deposition, so that deposition of nickel and iron species was done separately. This was done to remove the effect of anomalous co-deposition. The morphologies of electrodes fabricated in all experiments were characterised using scanning electron microscopy (SEM-JOEL JSM-7800F), and elemental mappings were obtained using energy dispersive X-Ray spectroscopy (X-Max50, large area 50 mm² Silicon Drift Detector, Oxford Instruments). Linear sweep voltammetry (LSV) and cyclic voltammetry (CV) were used as the electrochemical techniques to assess reaction kinetics for the OER. The voltammogram for LSV was obtained within the potential range of 0.2–1.2 V vs SCE, with a scan rate of 50 mV/s. The electrolyte used in the electrochemical characterisation was 0.1 M KOH at room temperature. Platinum wire and saturated calomel electrode (SCE) were used as counter and reference electrode, respectively. Chronoamperometry was used to assess the electrode stability, where a constant potential of 1.2 V vs SCE was applied to the working electrode in 4 sets with a duration of 15 h. Between each set, the working electrode was rinsed and dried to eliminate the adverse effect of bubble binding,

which increases charge transfer resistance, thereby providing false information on material stability performance. The electrolyte concentration used in the stability test was 10 g KOH in 1L water (approximately 0.178 M). The counter electrode used in the stability test was carbon rod.

2.1 Materials

All materials were used as acquired without further purification. Nickel sulfate ($\text{NiSO}_4 \cdot 6\text{H}_2\text{O}$, $\geq 98.0\%$ ACS reagent, Sigma-Aldrich), iron sulfate ($\text{FeSO}_4 \cdot 7\text{H}_2\text{O}$, $\geq 99.0\%$ ACS reagent, Sigma-Aldrich), sodium sulfate (Na_2SO_4 , $\geq 99.0\%$, anhydrous granular, Sigma-Aldrich) and 1 M sulfuric acid (H_2SO_4 , 99.999%, Sigma-Aldrich) are used. Nickel nitrate ($\text{Ni}(\text{NO}_3)_2 \cdot 6\text{H}_2\text{O}$, 98%, Alfa Aesar), iron nitrate ($\text{Fe}(\text{NO}_3)_3 \cdot 9\text{H}_2\text{O}$, $\geq 98\%$, Alfa Aesar) and potassium nitrate (KNO_3 , 99%, Alfa Aesar) are used. Nickel chloride ($\text{NiCl}_2 \cdot 6\text{H}_2\text{O}$, 98%, Alfa Aesar), ammonium chloride (NH_4Cl , $\geq 99.5\%$, Sigma-Aldrich), sodium chloride (NaCl , 99.99%, Alfa Aesar), ethylene glycol ($\text{C}_2\text{H}_6\text{O}_2$, 99%, Alfa Aesar) and iron sulfate ($\text{FeSO}_4 \cdot 7\text{H}_2\text{O}$, $\geq 99.0\%$ ACS reagent, Sigma-Aldrich) are used.

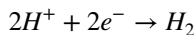
2.2 Electrodeposition with varying pH, deposition times and Ni^{2+} and Fe^{2+} concentrations

The deposition electrolyte was prepared by mixing the weighed mass of $\text{NiSO}_4 \cdot 6\text{H}_2\text{O}$ and $\text{FeSO}_4 \cdot 7\text{H}_2\text{O}$ in deionised water under stirring by a magnetic stirrer. Na_2SO_4 was also added as a supporting electrolyte. Once the salts were completely dissolved, 1 M H_2SO_4 was added dropwise using a plastic pipette under continuous stirring until the pH of the electrolyte solution dropped to 2, which was measured by the pH meter.

A piece of SS316 stripe was rinsed with acetone and IPA and then sonicated in deionised water for 30 min in an ultrasonic sound bath to remove surface impurities. After sonication, the SS316 stripe was rinsed with deionised water and left to dry. This cleaning procedure was the same for all following experiments.

The dried SS316 stripes were then submerged in the deposition electrolyte, which contained nickel and iron sulfate salts. The dimension of SS316 stripe submerged in electrolyte was 1.4 cm \times 2 cm (the total surface area was 5.6 cm² as the deposition took place on both sides of the stripe, and the surface area was the same for all experiments). A three-electrode system was employed for the electrodeposition process, using a constant potential of -1.3 V vs SCE applied to the working electrode for 300 s using a potentiostat (Ivium Compactstat–Ivium Technologies, Netherlands). The deposited SS316 electrode was then rinsed by deionised water and left to dry.

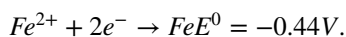
During the deposition reaction, H^+ ions were reduced to hydrogen in electrode/electrolyte interphase under acidic condition by the following reaction:



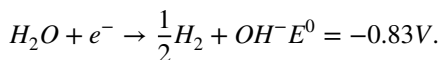
Simultaneously, Ni^{2+} present in electrolyte was transformed to adsorbed $\text{Ni}_{\text{ads}}^{2+}$ in electrode/electrolyte interphase, which acted as an intermediate for the formation of adsorbed hydrogen, H_{ads}^* . Chassaing suggested that when the pH of the sulphate deposition solution is between 2 and 4, the reaction that was associated with nickel electrocrystallisation was [30]:



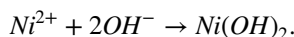
Similarly, Fe^{2+} is reduced to Fe by following reaction:



When the pH of the deposition is not adjusted, the solution was slightly acidic (~ 4.2), which was ascribed to the presence of nickel sulphate, that formed an acidic aqueous solution with pH 4.5. During the deposition process under this pH, the dominating reaction occurring in electrode/electrolyte interphase was the reduction of water:



The nickel hydroxide was produced by the reaction between adsorbed nickel and OH^- :



The purpose of this experiment is to look at the influence of pH, deposition time and salt concentrations on the performance of the nickel-based electrocatalysts coated on stainless-steel. There were five electrodes prepared in this experiment, of which the preparation conditions are given in Table 1.

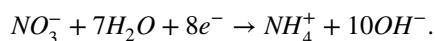
Table 1 Preparation conditions of electrodes 1 to 5, with different pHs and salt concentrations

Electrode number	Salt concentration (M)	pH of the electrolyte	Deposition time (seconds)	Deposition potential (V vs SCE)
1	0.025	2	300	-1.3 V
2	0.025	2	500	-1.3 V
3	0.05	2	300	-1.3 V
4	0.05	2	500	-1.3 V
5	0.025	4.2	300	-1.3 V

2.3 Electrodeposition with nitrate salts

The next set of experiments looked at the use of different salts. The main differences of electrodeposition conditions between the previous sets are as follows:

- (1) The metal salts used to make deposition solution are nickel nitrate and iron nitrate, instead of sulfate salts. This results in different reaction mechanisms to form the coating. With the presence of NO_3^- ions, the reduction reaction of NO_3^- will produce NH_4^+ and OH^- in the electrode and electrolyte interphase by the following reaction:



As a result, the OH^- ions react with Ni^{2+} and Fe^{3+} ions in solution, producing $\text{Ni}(\text{OH})_2$ and $\text{Fe}(\text{OH})_3$ on the electrode surface, which shows brown in colour. The reaction mechanism of film formation is



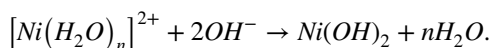
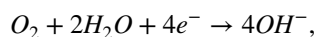
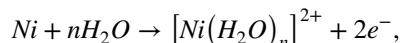
- (2) The deposition potentials used in this set of experiments are -1.3 V and -1.0 V vs SCE. The initial attempt of using -1.3 V generated poorly adherent film, and the potential was then adjusted to -1.0 V, at which significant improvement on film adherence was observed.
- (3) The pH effect of the deposition solution in this experiment was not investigated; therefore, no adjustment on pH was made.

The deposition electrolyte was prepared by mixing total amount of 0.05 M metal salts with varied ratio of Ni:Fe (1:1, 3:1, 6:1, and 9:1) under continuous stirring. 0.1 M KNO_3 was added as the supporting electrolyte. The cleaned SS316 stripe was submerged in an electrolyte bath. To investigate the effect of deposition potential, -1.3 V and -1.0 V vs SCE were applied to working electrodes for 300 s for all Ni:Fe ratios. The prepared electrodes were left to dry without rinsing with deionised water before the electrochemical characterisation, because of the poor material adhesion to the SS316 substrate.

2.4 Multi-step electrodeposition

This set of experiments was inspired by Wei et al., whose group proposed a NiFe-based material which they described as a ‘dendritic nickel tree with iron’ [29]. In the experiment, the material-coating process was split up into three steps. First, metallic nickel was deposited on a nickel foam substrate in slight acidic deposition conditions. The first coating process of nickel metal was followed by the hydrothermal

synthesis of $\text{Ni}(\text{OH})_2$ by water. According to their report [29], the reaction mechanisms of this step were shown as follows:



In the final step, the iron was deposited on the $\text{Ni}(\text{OH})_2$ formed on previous step to produce the NiFe electrode. The electrodes prepared at the end of each of three steps are referred to Ni metal, intermediate and Fe-doped Ni electrode.

The procedure was split in three steps:

- (1) Electrodeposition of Ni: the electrolyte was prepared by mixing 0.1 M $\text{NiCl}_2 \cdot 6\text{H}_2\text{O}$, 0.5 M NH_4Cl and 2 M NaCl. A constant potential of -1.0 V vs SCE was applied to the working electrode for 300 s. The electrode was rinsed by deionised water and left to dry.
- (2) Hydrothermal treatment: after drying, the hydrothermal treatment of the nickel-deposited electrode facilitated the formation of nickel hydroxide due to the weak oxidation in pure water, suggested by Wei et al. [29], who for the first time synthesised nickel hydroxide with water. The electrode prepared in step 1 was submerged in 50 ml deionised water in a PTFE Teflon reaction vessel, which was then heated at 150 °C for 5 h in a stainless-steel autoclave.
- (3) Fe incorporation: in the final step, 5 mmol FeSO_4 was dissolved in 30 ml ethylene glycol under nitrogen flow, and the solution was stirred for 10 min. The substrate prepared in step 2 was submerged into the solution in the Teflon vessel, which was then sealed in a stainless-steel autoclave and heated at 250 °C for 10 h. After the autoclave cooled down, the electrode was rinsed using a large amount of deionised water and dried in an oven at 60 °C.

2.5 Full electrolyser cell tests

The NiFe hydroxide prepared in the first set of experiments was selected as the anode for full-cell electrolyser testing. The setup of the electrolyser cell is shown in Figure S2 in Supporting Information. Two full electrolyser cells were built for the full-cell test. The first cell was made up of uncoated SS316 for both anode and cathode, and the second cell was made up of uncoated SS316 and an NiFe-coated electrode as cathode and anode, respectively. The electrodes were separated by a diaphragm. The electrolyte

Table 2 The ratio of each element presented in uncoated substrate, Electrodes 2 and 5 prepared in Experiment 1. It could be observed that the nickel content was much higher in coated electrodes, indicating successful deposition of nickel species, which improved the OER

Detected elements	Bare electrode	Electrode 2	Electrode 5
Fe	66.3%	63.1%	47.7%
Ni	9.6%	30%	35.1%
Cr	15.9%	2.1%	3.2%
C	5.2%	4.7%	4.7%
O	0	0	9.0%

concentration was 10 g KOH in 1 L of water. The electrolyte was delivered to the electrolyser cell by a pump via an inlet rubber tube, and the mixture of hydrogen, oxygen and electrolyte was delivered back to the electrolyte beaker via an outlet tube. The cyclic voltammogram of the full-cell electrolyser was measured between 0.6 and 2.0 V of cell voltage at room temperature, with a scan rate of 50 mV/s.

3 Results and discussion

3.1 Electrodeposition with varying pH, deposition times and Ni^{2+} and Fe^{2+} concentrations

The formation of $\text{Ni}(\text{OH})_2$ is supported by Lantelme's work [19], where the current density using potentiostatic deposition at different solution pHs was compared. The conclusion of Lantelme's work was that in unbuffered sulphate solution (pHs around 4.5), reduction of water occurred before any Ni^{2+} reduction could occur [31]. In addition, according to the impedance spectroscopy spectrum obtained by Holm and O'Keefe, when the pH of the sulphate solution increased to

3.5, the spectrum consisted of a semi-circle (charge transfer) and a vertical diffusion line, which could be attributed to the formation of a passivating nickel hydroxide layer [32]. These reactions explain the physical appearances of the obtained electrodes (see Fig S1 in Supporting Information). Electrodes 1–4 had a metal-like colour due to the formation of metallic nickel and iron, whereas electrode 5 had a darker colour, which was ascribed to the formation of a nickel hydroxide and iron hydroxide mixture.

Figure 1 shows the SEM images of electrode 2 (A and B) and electrode 5 (C and D), from which it is clearly evident that the pH and the changing deposition times affected the morphologies of the substrates. For the material grown in the low pH solution, the micrograph in Fig. 1 shows a grain-like structure of the material, which was grown under sufficiently fast mass transport and growth rate of Ni and Fe. For the material grown in the less acidic solution, the micrograph in Fig. 1 shows a flower-like image due to different reaction mechanisms that occurred on the electrode and electrolyte interphase. The EDS mappings show the elemental distribution in electrode 2 (Fig. 1) and Electrode 5 (Fig. 2A), showing that electrode 2 has a very homogeneous coverage of nickel and iron. The areas shown in Fig. 1G, H indicate that both coverage of iron and nickel is dense in this electrode. The map of chromium is not as compact as nickel and iron because a significant area of the substrate is covered underneath by electrodeposited nickel and iron. These conclusions are confirmed in the EDS map spectrum, from which the percentage abundance of each element was obtained (see Table 2). For electrode 2, the region shown in Fig. 1E) consisted of 63.1% Fe, 30% Ni, and 2.1% Cr, which indicates successful deposition of nickel and iron. Electrode 5 also has evenly distributed nickel and iron content, as well as a reduced chromium content due to the coverage of deposited nickel and iron. Furthermore, a significant amount of

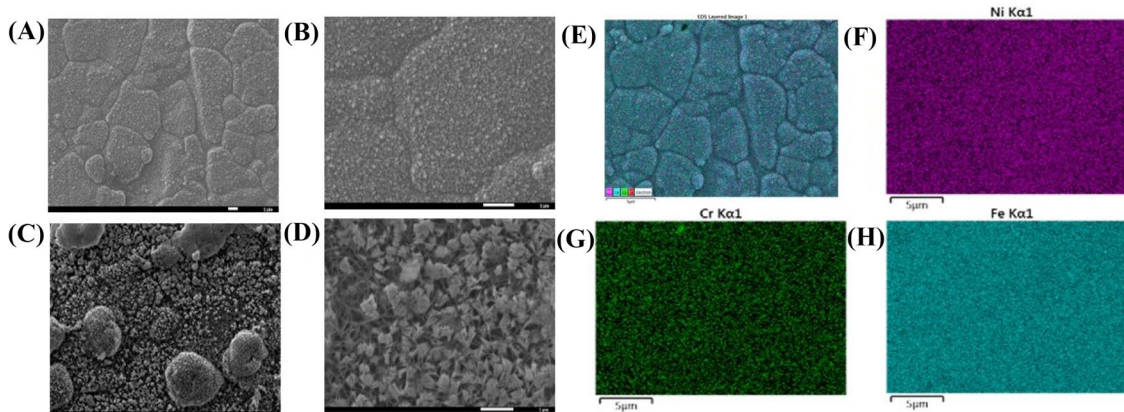
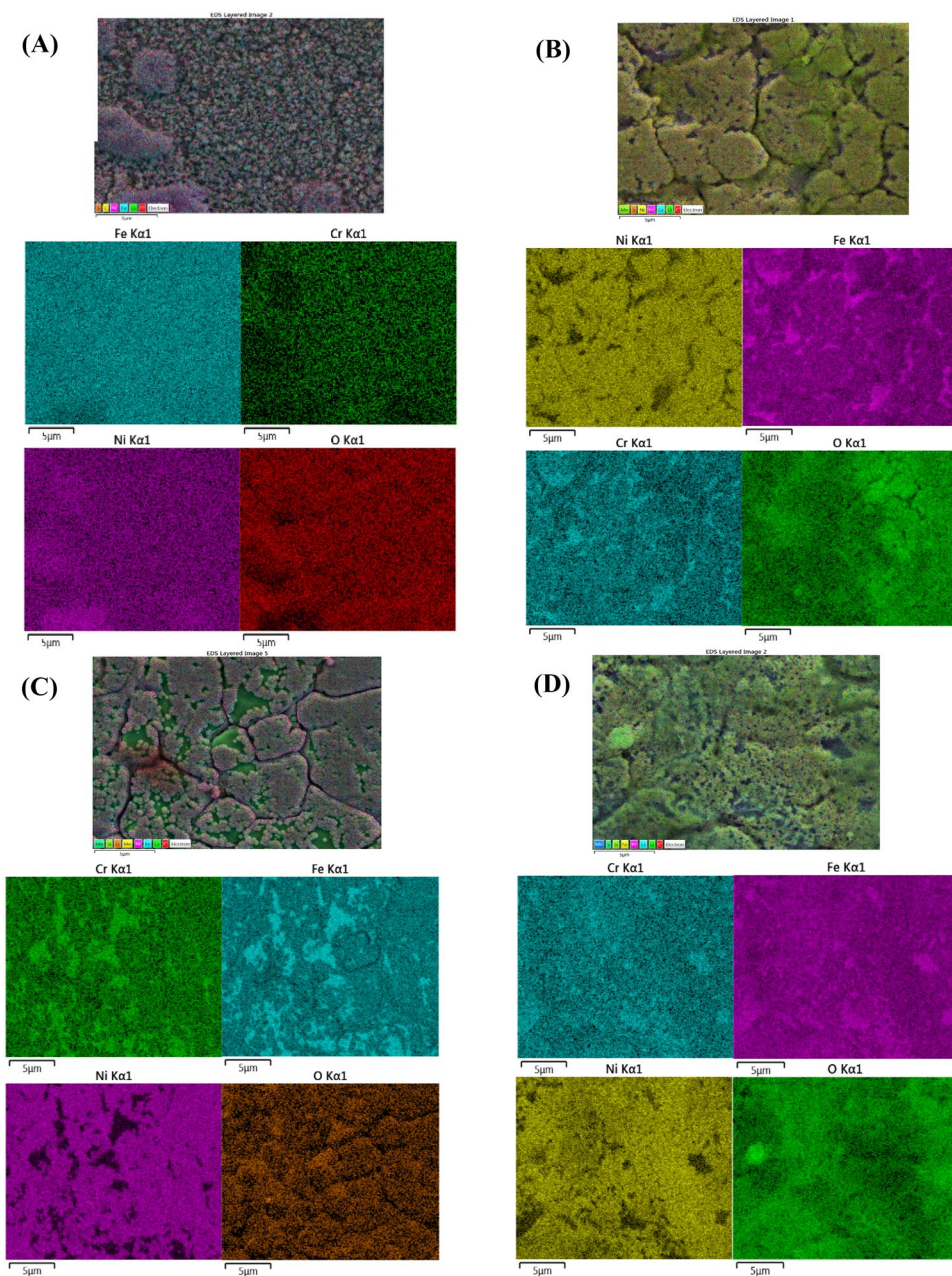


Fig. 1 SEM images of (A) electrode 2 with a 2,000 magnification, B electrode 2 with a 10,000 magnification, C electrode 5 with a 2,000 magnification and D electrode 5 with a 10,000 magnification. E–H

Elemental analysis of the micrograph in (A) showing coverage of nickel (F), chromium (G) and iron (H)

Fig. 2 EDS mapping of (A) Electrode 5 in Experiment 1. The sample showed the presence of Fe, Cr, Ni, and O, indicating that Ni and Fe were successfully deposited on the substrate in its (hydr)oxide form; (B) Ni-coated electrode prepared in the electrodeposition of Ni step of Experiment 3. The sample showed Ni enrichment; (C) Hydrothermal treatment step of Experiment 3. It is obvious that the material deposited in the electrodeposition of Ni step was broken down by water under high pressure and temperature, indicating that the morphology was not successfully controlled, and the sample exhibited reduced OER activity due to the loss of catalytic material. However, it could potentially increase the coating porosity which could give an improved charge transfer path and enhanced OER activity if this step can be optimised; (D) Fe incorporation step of Experiment 3



oxygen was detected, which could potentially evidence the formation of NiFe hydroxide.

The ratios of nickel and iron shown in Table 2 do not reflect the composition of coating materials formed by the electrodeposition process. The reason is that detected nickel and iron contents by EDS are the sum of these elements in both coating and bare substrate. Moreover, the electrodeposition process is believed to consist of anomalous co-deposition, during which processes, the reduction rate of more active species is faster than that of less active species [33]. In this experiment, the rate of $\text{Fe}^{2+} \rightarrow \text{Fe}$ was faster than that of $\text{Ni}^{2+} \rightarrow \text{Ni}$. As a consequence, it is assumed that

the composition of the more active Fe formed by the electrodeposition process was higher than that of Ni [34].

The linear sweep voltammogram of electrodes 1 to 5 and of the uncoated stainless-steel substrate are presented in Fig. 3. The figure shows significant improvement on OER on the coated electrodes compared to uncoated substrate (black line). Electrode 5 is the best performing electrode, with the lowest onset potential and the lowest overpotential for an equal current density. For instance, at 1.2 V vs SCE, the current density generated by electrode 5 is 55 mA cm^{-2} . Electrodes 2, 3 and 4 had lower current densities, which ranged between 48 and 50 mA cm^{-2} at the same potentials. Electrode 1 generates a much lower current density of

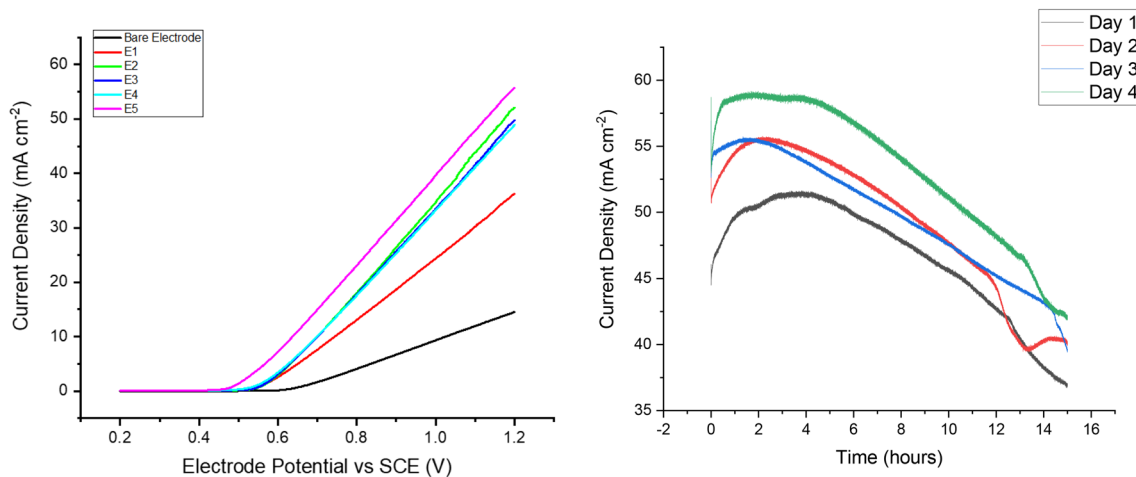


Fig. 3 Linear Sweep Voltammograms of electrodes 1 to 5 and of the uncoated stainless-steel electrode (left) tested in 0.1 M KOH electrolyte. The applied potential was 0.2–1.2 V vs SCE, with a scan rate of

50 mV/s. Chronoamperometry of electrode 5 to test stability (right). The electrolyte concentration used in the stability test was 0.178 M KOH (10 g KOH dissolved in 1L deionised water)

Table 3 Electrochemical characterisation results (LSV) of Electrodes 1–5 and uncoated electrode. The table shows the peak current density in mA cm^{-2} when cell potential is 1.2 V vs SCE and overpotential in mV at benchmark current density of 10 mA cm^{-2}

Electrode type	Current density at 1.2 V vs SCE (mA cm^{-2})	Overpotential vs SHE at 10 mA cm^{-2} (mV)
Electrode 1	35	574
Electrode 2	52	620
Electrode 3	49	624
Electrode 4	48	624
Electrode 5	56	514
Uncoated stainless-steel substrate	15	844

35 mA cm^{-2} at the same potential. The uncoated electrode only produces 15 mA cm^{-2} at 1.2 V vs SCE. Besides an increased current density, improved OER kinetics in electrodes 1 to 5 are also exhibited by lower overpotentials at 10 mA cm^{-2} , which indicates that the energy consumption that triggers the OER is lower in the coated electrodes. As seen in Fig. 3, the potential of electrode 5 at 10 mA cm^{-2} is 0.67 V vs SCE. According to the half-reaction of OER, the standard electrode potential for the OER is 0.4 V (at 25°C and under $\text{pH} = 14$) [35]. Therefore, the overpotential of electrode 5 is 514 mV vs SHE (given that the potential of SCE is 0.244 V vs SCE at 25°C). Electrodes 2, 3 and 4 have similar overpotentials of 624 mV vs SHE at 10 mA cm^{-2} . Electrode 1 has a higher overpotential of 574 mV vs SHE. The uncoated substrate has a very high overpotential of 844 mV vs SHE. The summarised electrochemical data are presented in Table 3.

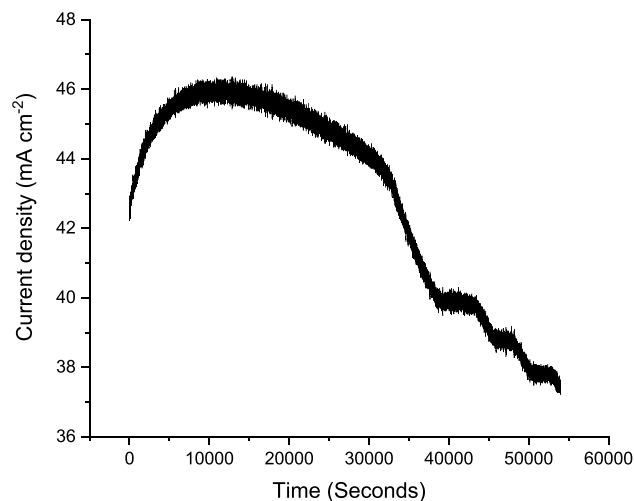


Fig. 4 Uncoated SS316 stability test reveals that the uncoated electrode loses current density quickly halfway through the test

Same as bare stainless steel, NiFe-deposited electrodes also undergo degradation during their operation in alkaline environment; therefore, the rate of degradation is also a key parameter to ensure a good overall performance of the electrolyser. In order to evaluate this, stability tests are performed using chronoamperometry on the best performing electrode (Electrode 5) and are presented in Fig. 3. The figure shows that the current density increased during the first 10,000 to 15,000 s, where it peaked, and decreased continuously after this. This trend was repeated for all tests on subsequent days. In each day, the initial increase of current density until 15,000 s was likely the result of a phase transformation from $\beta\text{-Ni}(\text{OH})_2$ to $\beta\text{-NiOOH}$ and diffusion

of OH^- ions to active sites of NiOOH until the maximum number of active sites is occupied during the reaction. Afterwards, the resistive effect of gas bubbles that were formed started to increase the overall impedance and hindered further charge transfer, thereby decreasing the current density. The reduced current density could be ascribed to bubble-binding effect and areaction–diffusion layer instead of electrode degradation. The evidence was that the starting current density on each day was always higher than that of the previous day, which was also a sign of activation of the catalytic material, i.e. more $\beta\text{-Ni}(\text{OH})_2$ is converted to the more active $\beta\text{-NiOOH}$ phase.

The chronoamperometry was also performed to bare stainless steel (Fig. 4), which showed an increase in current density until 10,000 s, which can be the result of the oxidation of metallic nickel in stainless steel that improves the OER.

After peak density was reached, it started to decrease steadily until 30,000 s. A significant reduction of current density was observed between 30,000 and 40,000 s. This reduction was not observed on the coated electrode, which was a further sign that stability was also improved by coating.

3.2 Electrodeposition with nitrate salts

The SEM images in Fig. 5A–D show the morphologies of coatings deposited at -1.0 V and -1.3 V, where the Ni:Fe ratio is 3:1. The most significant observation in the two SEM images is that when the deposition potential of -1.0 V was used, there was an even distribution of small micron-scale particles. However, when -1.3 V was used, large areas of the stainless-steel substrate were observable, which suggested that a poorly deposited layer was formed with low-material loading (shown in red circles).

Poor adhesion and flaking of coating materials were the main issues when using nickel nitrate and iron nitrate

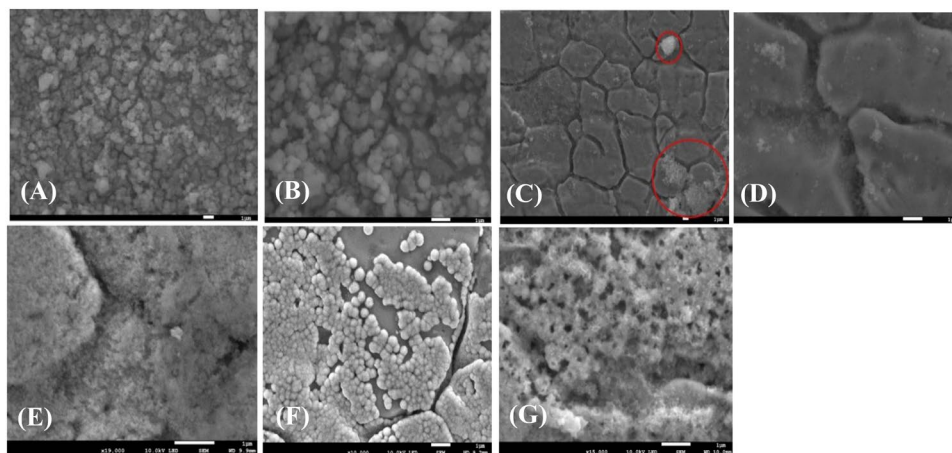
solutions as the deposition electrolyte, in particular when highly negative potentials, e.g. -1.3 V, were used. The poor adhesion was likely caused by high HER rate, which produced more H_2 gas bubbles that adversely affected the formation of nickel hydroxide on the electrode surface. In addition, the EDS analysis showed that when -1.0 V was used, the Ni loading was twice as much as when -1.3 V was used, indicating the loss of coating material during rinsing by deionised water after deposition.

The linear sweep voltammograms of all electrodes prepared in the second set of experiments are shown in Fig. 6. The electrochemical data are shown in Table 4.

The peak current densities of all electrodes were within the range of $20\text{--}40\text{ mA cm}^{-2}$ and much improved compared to peak current densities produced by bare stainless steel. As Fig. 6 shows, NiFe 6–1 (-1.3 V) and NiFe 1–1 (-1.3 V) exhibited much higher current densities than other electrodes. However, no correlation was found between Ni:Fe ratio and current density. Poor electrochemical performance of electrodes prepared under -1.0 V was likely caused by a thick material layer and high charge transfer resistance. The SEM images of electrodes prepared at -1.0 V Fig. 5A, B suggested that the substantial coverage of the dense coating was present on the substrate, meaning that charge transfer of the electrochemical process was difficult to occur.

NiFe 6–1 (-1.3 V) is selected for the stability test, as it was the electrode with the highest current density at 1.2 V vs SCE. The test conditions and methods for the chronoamperometry stability test were the same as those used in the first set of experiments, in which the potential was held at 1.2 V vs SCE for four consecutive days, with a 15 h duration in each day in 0.178 M KOH (10 g KOH in 1L water). The stability test results in Fig. 6 show that the current density of in every day increases during the first 10,000 s and then starts to lose current until the end of the day. The current density reached the maximum on day 2 and declined in subsequent days. The enhancement of OER by NiFe 6–1 (-1.3 V)

Fig. 5 SEM images of (A) Ni:Fe 3:1– 1.0 V with 2000 magnification; (B) Ni:Fe 3:1– 1.0 V with 10,000 magnification; (C) Ni:Fe 3:1– 1.3 V with 20,000 magnification; (D) Ni:Fe 3:1– 1.3 V with 10,000 magnification; Both electrodes were prepared in Experiment 2; (E) Electrodeposition of Ni; (F) Hydrothermal treatment; (G) Fe incorporation; All samples of (E–G) were prepared in Experiment 3



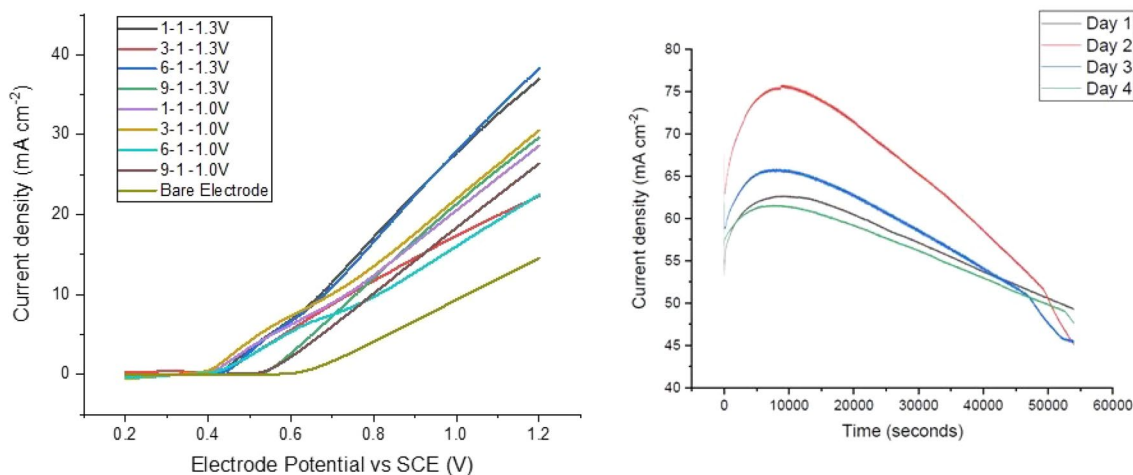


Fig. 6 LSV of all electrodes and of the uncoated electrode from the second set of experiments using nickel and iron nitrate salts (left). The captions refer to the ratios used for Ni and Fe and the deposition potentials. Stability test result (chronoamperometry) of NiFe 6–1 (– 1.3 V) (right). The loss of activity is clearly evident, as a result of poor adhesion of catalytic coating. The LSV was measured between

0.2 and 1.2 V vs SCE, with 50 mV/s scan rate in 0.1 M KOH electrolyte concentration. The chronoamperometry was performed on electrode 6–1 (– 1.3 V) at 1.2 V vs SCE for 4 consecutive days, 15 h each day. The electrolyte concentration used in stability test was 0.178 M KOH

Table 4 Electrochemical characterisation results (LSV) for the electrodes produced using different salts

Electrodes	Current density at 1.2 V vs SCE (mA cm ⁻²)	Overpotential vs SHE at 10 mA cm ⁻² (mV)
NiFe 1–1 (– 1.3 V)	36	671
NiFe 3–1 (– 1.3 V)	24	741
NiFe 6–1 (– 1.3 V)	39	681
NiFe 9–1 (– 1.3 V)	28	757
NiFe 1–1 (– 1.0 V)	28	735
NiFe 3–1 (– 1.0 V)	30	698
NiFe 6–1 (– 1.0 V)	24	811
NiFe 9–1 (– 1.0 V)	29	798
Stainless steel	15	844

followed the same mechanisms of α -Ni(OH)₂ to β -NiOOH conversion as in the first set of experiments. Although the current density of NiFe 6–1 (– 1.3 V) was higher than the electrode used for the first stability test (Fig. 3), the biggest disadvantage of NiFe 6–1 (– 1.3 V) was that current density reduced more rapidly over 60 h of stability test, revealing the loss of OER activity. In addition to bubble blinding, loss of catalytic material was another cause of reduction of OER activity. At the end of the stability test, flaked-off coating material was observable at the bottom of the electrolyte flask.

As a conclusion for the set of experiments with nickel and iron nitrate salts, the prepared electrodes all exhibited improvements on the OER compared to bare stainless steel, which was reflected by the reduced overpotential at a current

Table 5 The ratio of each element presented in uncoated substrate and all three samples prepared in Experiment 3. From the Experiment 3, nickel loading reached more than 50%, which suggested that this is a promising technique which can be further studied to enable its potential as OER catalyst

Detected elements	Bare electrode	Ni-coated electrode	Intermediate	Fe-doped nickel-coated electrode
Fe	66.3%	21.5%	25%	35.3%
Ni	9.6%	53.2%	58.6%	42.1%
Cr	15.9%	5.8%	6.7%	8%
C	5.2%	11.2%	7.6%	5.1%
O	0	7.4%	1%	8.1%

density of 10 mA cm⁻². However, based on the LSV results, the improvement was not significant enough to be used in scaled-up commercial electrolyzers. Moreover, all electrodes suffered from poor material adhesion and low charge transfer kinetics. In addition, material flaking caused rapid loss of OER activity. This could have been minimised by optimising experimental parameters such as deposition time, temperature, and Ni to Fe ratio, in order to further improve the material adhesion on the substrate, OER activity and stability.

3.3 Multi-step electrodeposition

Figure 5E-G shows the SEM images of Ni-coated electrode (A), intermediate (B) and Fe-doped Ni electrode (C). From the figure, a full coating coverage can be observed. After water treatment under higher temperatures and pressures,

coating break up was evident and showed spherical agglomerate-like features. The exposed area of the stainless-steel substrate indicated that coating losses occurred during this step. Finally, after the last step, another layer of coating was successfully deposited. The EDS mappings of Ni-coated electrode, intermediate and Fe-doped Ni electrode are shown in Fig. 2B, D. The elemental compositions of all three electrodes are shown in Table 5. The EDS mappings of all three electrodes suggest that the coating material is very nickel rich. Moreover, the Ni content in the Fe-doped nickel-coated electrode is larger than the Fe content, which indicated successful elimination of the anomalous co-deposition effect. The results for the linear sweep voltammetry on the electrodes produced using the multistep electrodeposition are shown in Fig. 7.

The LSV graph shown in Fig. 7 showed that both nickel-coated and intermediate only enhanced OER by a small degree, whereas the Fe-doped nickel-coated electrode produced after the final step showed a much more marked improvement in OER. For the Ni-coated electrode, there was a noticeable anodic peak occurring at 0.4 V vs SCE that indicated the oxidation of Ni/Ni oxide to nickel oxyhydroxide, which involved increasing the oxidation states of the nickel species. After treatment in water (sample shown

alone. The quantified electrochemical performance of all three electrodes is shown in Table 6.

The electrode prepared after the final step, the Fe-doped Ni-coated electrode, was selected for the stability test, which was done following the same procedures and conditions as the previous stability tests. The plot for each day followed the same trend, which was that the current density increased during the first 5000 s, then reduced until the end of the test. The current density increased dramatically on day 2 onwards, which could be the result of activation and sufficient transformation of the OER-active species, γ -NiOOH. There was no further increase of current density on days 3 and 4, which indicated that the coating material was fully activated and transformed during day 1. In addition, there was no sign of a performance decline between day 2 to day 4, which indicated that the Fe-doped Ni-coated electrode exhibited good stability in alkaline conditions. This indicates that the current density reduction on each individual day could be fully explained by bubble binding, which resulted in a lower charge transfer rate. However, at the beginning of day 3 and 4, interrupted charge transfer could be observed on the regions of current density fluctuation, which was possibly the cause for increased charge transfer resistance.

As a conclusion for the multistep electrodeposition exper-

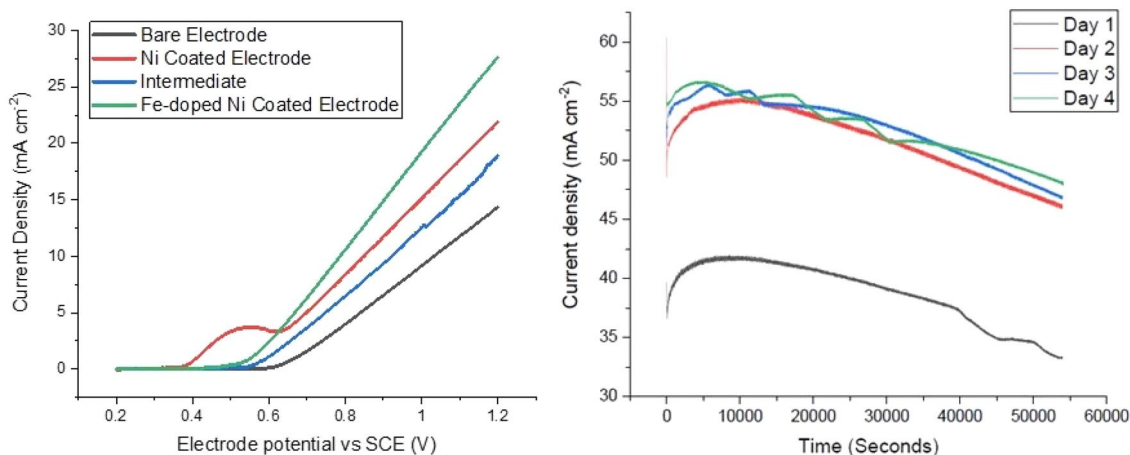


Fig. 7 Electrochemical characterisation results of electrodes prepared in this set of experiments. LSV (left) was measured between 0.2 and 1.2 V vs SCE with scan rate of 50 mV/s in 0.1 M KOH. The chrono-

amperometry was performed at 1.2 V vs SCE for 4 consecutive days, 15 h each day (right). The electrolyte concentration used in stability test was 0.178 M KOH

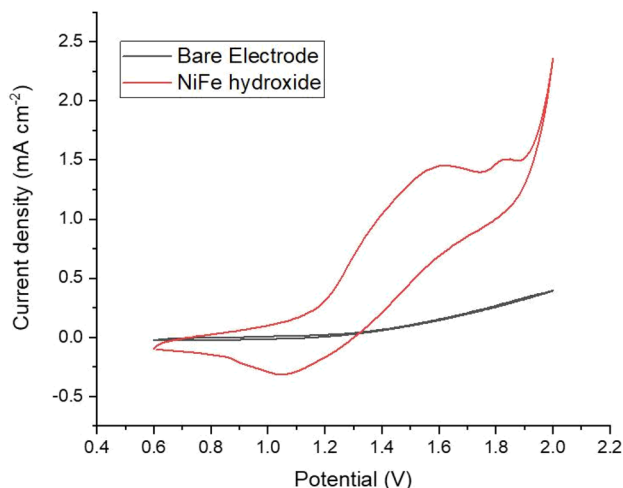
amperometry was performed at 1.2 V vs SCE for 4 consecutive days, 15 h each day (right). The electrolyte concentration used in stability test was 0.178 M KOH

intermediate (blue), the reaction reported by Wei et al. [29], in which metallic nickel was transformed to nickel hydroxide by the weak oxidation power of water, was not evident on the stainless-steel substrate. The intermediate electrode exhibited slightly lower OER activity; however, when a small amount of Fe was added to the nickel coating, the improved OER activity could be observed and the performance of Fe-doped Ni-coated electrode was better than the Ni-coated electrode

improvements, the Fe-doped Ni-coated electrode improved the OER activity compared to bare stainless steel, both in terms of peak current density and overpotential at 10 mA cm^{-2} . The coating process took longer processing times than the single-step electrodeposition because of its multistep preparation method. Based on EDS data, the electrode preparation successfully avoided the effect of anomalous co-deposition, which resulted in a lower Fe content compared with Ni in

Table 6 The summarised electrochemical characterisation results (LSV) of the electrodes using multistep electrodeposition and the uncoated substrate

Electrodes	Current density at 1.2 V vs SCE (mA cm^{-2})	Overpotential vs SHE at 10 mA cm^{-2} (mV)
Ni-coated electrode	22	698
Intermediate	18	770
Fe-doped Ni-coated electrode	27	635
Bare stainless steel	15	848

**Fig. 8** Cyclic voltammogram of a full-cell electrolyser with NiFe hydroxide-coated anode (red) and uncoated anode (black). The red plot shows peaks between 1.5 and 1.8 V, which indicates phase transformation of the coating material. The OER occurred at 1.9 V. The uncoated electrode shows neither evident phase transformation nor significant OER peaks, therefore making it difficult to identify the starting potential of the uncoated electrode within the used voltage range

the coating material. The stability results also suggest that the Fe-doped nickel-coated electrode exhibited excellent stability, therefore, showing that this material could be attractive as an anode material for industrial-scale alkaline water electrolyzers.

3.4 Full electrolyser cell tests

The cyclic voltammogram of the full-cell electrolyser, which is made up of coated and uncoated anodes and was measured between 0.6 and 2.0 V of cell voltage is shown in Fig. 8. The peaks observed in the red line between 1.2 and 1.6 V correspond to the reversible phase transformation from $\beta\text{-Ni(OH)}_2$ to $\beta\text{-NiOOH}$ and $\gamma\text{-NiOOH}$. Its reverse reaction occurred when the cyclic voltammetry scanned backwards towards lower potential, which was indicated by the peak where the potential was 1.1 V. The small oxidation peak observed between approximately 1.7–1.9 V corresponds to the further oxidation of $\beta\text{-NiOOH}$ to $\gamma\text{-NiOOH}$, which was an irreversible phase transformation; therefore, there was no

evident reduction peak observed for such reaction. The OER onset potential was approximately 1.9 V. In contrast, the bare stainless-steel anode did not have any evident peaks that indicated phase transformation, and only generated a small current density within the scanned voltage range (Fig. 8, black line). Therefore, it was difficult to accurately determine the OER onset potential for the bare stainless-steel anode. The OER onset potential for the NiFe-coated electrode was evident in the cyclic voltammogram and could be easily determined. At 2.0 V cell potential, the NiFe-coated electrode generated nearly six times as much current density as the uncoated electrode. These conclusions overall suggest that the NiFe-coated anode exhibited higher OER reaction kinetics and lower overpotentials than the uncoated anode, thereby improving the performance.

4 Conclusions

Based on electrochemical results of half-cell tests, catalytic-coated electrodes for alkaline water electrolysis were successfully fabricated from all three sets of experiments. The half-cell data suggested that coated electrodes generated much higher current density than uncoated stainless-steel electrodes. Furthermore, lower overpotentials at 10 mA cm^{-2} were observed for coated electrodes. It is expected that these coatings can help achieve much higher electrical efficiency if operated under their optimal operating conditions. The stability tests of all experiments suggested a much-improved stability in contrast to the uncoated electrodes; however, the stability test needs to be operated for longer periods and under harsh operating conditions in order to assess whether the coated anode enables their electrolyzers to achieve target performance specifications.

In recent decades, a lot of developmental work has been devoted to alkaline water electrolyzers in order to improve their overall performance. Based on the work outlined above, there are a number of points that can be considered to enhance the performance of alkaline water electrolyzers in terms of energy consumption and electrical efficiency.

(1) Morphology control

In order to use the maximum available active sites of a catalyst, innovative design and synthesis of nano-

structured catalytic materials are crucial. Furthermore, with appropriate morphology, the catalytic materials would ease charge transfer and have shorter pathways for ion diffusion.

- (2) Investigation on various dopants and optimisation of the Ni-to-dopant ratio

Although many researchers have proved that doping trace amounts of Fe impurity by either deliberately contaminating the electrolyte or adding it to Ni-based catalysts could improve overall OER activity, there is still a lack of comprehensive understanding on the role of the dopant. Some effort was devoted to this investigation, for instance, Li et al. concluded that the state valency of Ni increases by 0.5 for 5–10% Fe incorporation. The role of Fe in Ni-based catalysts promotes the formation of $\text{Ni}^{3+/4+}$ and oxyl character, which are beneficial to improve the overall OER activity in Ni oxidic catalysts [44]. Similar conclusions were also made recently by Anantharaj et al., who found that Fe^{3+} incorporation suppresses metal oxidation and facilitates OER. Furthermore, the Lewis acidity effect of Fe^{3+} promotes the oxidation of Ni^{3+} to Ni^{4+} in NiOOH , which matches the conclusion made by Li et al. [41].

- (3) Reduction of overpotential

The overpotential of the electrolyser is directly linked to polarisation and ohmic resistances. The overpotential related to polarisation resistance, V_{act} , is related to the effect of the electrical double layer. The ohmic resistance is usually contributed to by gas bubbles produced during reaction, and ionic conductivity is affected by parameters such as the electrolyte and catalytic materials. Unfortunately, NiFe-based hydroxides have poor conductivity. Common conductive additives such as carbon black and carbon nanotubes cause issues related to carbonate impurities and cost. The electrolyte resistance can be minimised by optimisation of the electrode gap, e.g., a zero-gap configuration can be a solution. Finally, efficient gas bubble removal can be achieved by designing a 3D electrode structure. As a planar 2D structure, stainless-steel plates have poor gas removal ability, which could be aggravated when a layer of catalytic film is deposited.

Supplementary Information The online version contains supplementary material available at <https://doi.org/10.1007/s10800-022-01817-4>.

Acknowledgements This work was funded by Centre for Global Eco-Innovation and Clean Power Hydrogen Ltd.

Funding This work was funded by Centre for Global Eco-Innovation, Clean Power Hydrogen Ltd

Declarations

Conflict of interest Clean Power Hydrogen Group, which funded the research and employs NW, has commercial interests in electrolysers and hydrogen technologies.

Open Access This article is licensed under a Creative Commons Attribution 4.0 International License, which permits use, sharing, adaptation, distribution and reproduction in any medium or format, as long as you give appropriate credit to the original author(s) and the source, provide a link to the Creative Commons licence, and indicate if changes were made. The images or other third party material in this article are included in the article's Creative Commons licence, unless indicated otherwise in a credit line to the material. If material is not included in the article's Creative Commons licence and your intended use is not permitted by statutory regulation or exceeds the permitted use, you will need to obtain permission directly from the copyright holder. To view a copy of this licence, visit <http://creativecommons.org/licenses/by/4.0/>.

References

- Liu K (2010) Hydrogen and syngas production and purification technologies. Wiley, Hoboken, NJ
- Brauns J, Turek T (2020) Alkaline water electrolysis powered by renewable energy: a review. *Processes* 8(2):248
- IEA. (2021) The Future of Hydrogen – Analysis - IEA. Available at: <<https://www.iea.org/reports/the-future-of-hydrogen#>> Accessed 23 October 2021
- Guo Y et al (2019) Comparison between hydrogen production by alkaline water electrolysis and hydrogen production by PEM electrolysis. *IOP Conf Ser: Earth Environ Sci.* <https://doi.org/10.1088/1755-1315/371/4/042022>
- Kuckshinrichs W, Ketelaer T, Koj J (2017) Economic analysis of improved alkaline water electrolysis. *Front Energy Res.* <https://doi.org/10.3389/fenrg.2017.00001/full%3e>
- Guo Y, Li G, Zhou J, Liu Y (2019) Comparison between hydrogen production by alkaline water electrolysis and hydrogen production by PEM electrolysis. *IOP IOP Conf Ser: Earth Environ Sci.* <https://doi.org/10.1088/1755-1315/371/4/042022/pdf>
- Zayat, B., Mitra, D., Irshad, A., Rajan, A. and Narayanan, S., (2021) Inexpensive and robust iron-based electrode substrates for water electrolysis and energy storage. *Current Opinion in Electrochemistry*, 25, p.100628. Available at: <<https://www.sciencedirect.com/science/article/abs/pii/S2451910320301630>>
- Sivanantham, A. and Shanmugam, S., (2017) Nickel selenide supported on nickel foam as an efficient and durable non-precious electrocatalyst for the alkaline water electrolysis. *Applied Catalysis B: Environmental*, 203, pp.485–493. Available at: <https://www.sciencedirect.com/science/article/abs/pii/S0926337316308141?casa_token=jZmE-OAU7ZgAAAAA:p2R6CHhWY5yL2Z186YLBGCpLfqqqkmu-DO1P7SBvVyAcftiYau_KHiCJWEw1SFHedpSd1GHIFQ>
- Trotochaud L, Young S, Ranney J, Boettcher S (2014) Nickel-Iron oxyhydroxide oxygen-evolution electrocatalysts: the role of intentional and incidental iron incorporation. *J Am Chem Soc.* <https://doi.org/10.1021/ja502379c>
- Vij V, Sultan S, Harzandi A, Meena A, Tiwari J, Lee W, Yoon T, Kim K (2017) Nickel-based electrocatalysts for energy-related applications: oxygen reduction oxygen evolution, and hydrogen evolution reactions. *ACS Catal.* <https://doi.org/10.1021/acscatal.7b01800>
- Nickelinstitute.org. 2021. Stainless steel: The role of nickel | Nickel Institute. [online] Available at: <<https://nickelinstitute.org/about-nickel/stainless-steel/>> Accessed 23 October 2021

12. Anantharaj S, Venkatesh M, Salunke A, Simha T, Prabu V, Kundu S (2017) High-performance oxygen evolution anode from stainless steel via controlled surface oxidation and Cr removal. *ACS Sustain Chem Eng*. <https://doi.org/10.1021/acssuschemeng.7b02090>
13. Schäfer, H., Sadaf, S., Walder, L., Kuepper, K., Dinklage, S., Wollschläger, J., Schneider, L., Steinhart, M., Hardege, J. and Daum, D., (2015) Stainless steel made to rust: a robust water-splitting catalyst with benchmark characteristics. *Energy & Environmental Science*, 8(9), pp.2685–2697. Available at: <https://pubs.rsc.org/en/content/articlelanding/2015/ee/c5ee01601k>
14. Schäfer H, Beladi-Mousavi S, Walder L, Wollschläger J, Kuschel O, Ichilmann S, Sadaf S, Steinhart M, Küpper K, Schneider L (2015) Surface oxidation of stainless steel: oxygen evolution electrocatalysts with high catalytic activity. *ACS Catal*. <https://doi.org/10.1021/acscatal.5b00221>
15. Zhong H, Wang J, Meng F, Zhang X (2016) In situ activating ubiquitous rust towards low-cost, efficient, free-standing, and recoverable oxygen evolution electrodes. *Angew Chem Int Ed*. <https://doi.org/10.1002/anie.201604040>
16. Wang, S., Lu, A. and Zhong, C., (2021) Hydrogen production from water electrolysis: role of catalysts. *Nano Convergence*, 8(1). Available at: <https://www.citethisforme.com/cite/journal/autocite> Accessed 23 October 2021
17. Suen, N., Hung, S., Quan, Q., Zhang, N., Xu, Y. and Chen, H., (2017) Electrocatalysis for the oxygen evolution reaction: recent development and future perspectives. *Chemical Society Reviews*, 46(2), pp.337–365. Available at: <https://pubs.rsc.org/en/content/articlelanding/2017/CS/C6CS00328A#!divCitation>
18. Valdés Á, Brilllet J, Grätzel M, Gudmundsdóttir H, Hansen H, Jónsson H, Klüpfel P, Kroes G, Le Formal F, Man I, Martins R, Nørskov J, Rossmeisl J, Sivula K, Vojvodic A, Zäch M (2012) Solar hydrogen production with semiconductor metal oxides: new directions in experiment and theory. *Phys Chem Chem Phys* 14(1):49–70
19. Wang R, Chen Z, Hu N, Xu C, Shen Z, Liu J (2018) Nanocarbon-based electrocatalysts for rechargeable aqueous Li/Zn-air batteries. *ChemElectroChem*. <https://doi.org/10.1002/celec.201800141>
20. Fabbri, E., Haberer, A., Waltar, K., Kötz, R. and Schmidt, T., (2014) Developments and perspectives of oxide-based catalysts for the oxygen evolution reaction. *Catal. Sci. Technol.*, 4(11), pp.3800–3821. Available at: <https://pubs.rsc.org/en/content/articlehtml/2014/cy/c4cy00669k>
21. Yue, X., Jin, Y. and Shen, P., (2017) Highly stable and efficient non-precious metal electrocatalysts of tantalum dioxide used for the oxygen evolution reaction. *Journal of Materials Chemistry A*, 5(18), pp.8287–8291. Available at: <https://pubs.rsc.org/en/content/articlelanding/2017/ta/c7ta01838j#!divAbstract>
22. Zheng Y, Jiao Y, Li L, Xing T, Chen Y, Jaroniec M, Qiao S (2014) Toward design of synergistically active carbon-based catalysts for electrocatalytic hydrogen evolution. *ACS Nano*. <https://doi.org/10.1021/nn501434a>
23. Suen, N., Hung, S., Quan, Q., Zhang, N., Xu, Y. and Chen, H. 2017 Electrocatalysis for the oxygen evolution reaction: recent development and future perspectives. *Chemical Society Reviews*, 46(2), pp.337–365. Available at: <https://pubs.rsc.org/en/content/articlelanding/2017/cs/c6cs00328a#!divAbstract> Accessed 18 Feb. 2019
24. Zayat B, Mitra D, Narayanan S (2020) Inexpensive and efficient alkaline water electrolyzer with robust steel-based electrodes. *J Electrochem Soc*. <https://doi.org/10.1149/1945-7111/aba792>
25. Yu M, Budiyo E, Tüysüz H (2021) Principles of water electrolysis and recent progress in Cobalt-, Nickel-, and Iron-based oxides for the oxygen evolution reaction. *Angew Chemie Int Ed*. <https://doi.org/10.1002/anie.202103824>
26. Qu, H., He, X., Wang, Y. and Hou, S., (2021) Electrocatalysis for the Oxygen Evolution Reaction in Acidic Media: Progress and Challenges. *Applied Sciences*, 11(10), p.4320. Available at: <https://www.mdpi.com/2076-3417/11/10/4320>
27. Babar N, Joya K (2020) Spray-coated thin-film Ni-oxide nanoflakes as single electrocatalysts for oxygen evolution and hydrogen generation from water Splitting. *ACS Omega*. <https://doi.org/10.1021/acsomega.9b02960>
28. Dong G, Fang M, Zhang J, Wei R, Shu L, Liang X, Yip S, Wang F, Guan L, Zheng Z, Ho J (2017) In situ formation of highly active Ni–Fe based oxygen-evolving electrocatalysts via simple reactive dip-coating. *J Mater Chem A* 5(22):11009–11015
29. Wei, W., He, W., Shi, B., Dong, G., Lu, X., Zeng, M., Gao, X., Wang, Q., Zhou, G., Liu, J., Herczynski, A., Kempa, K. and Gao, J., (2019) A bio-inspired 3D quasi-fractal nanostructure for an improved oxygen evolution reaction. *Chemical Communications*, 55(3), pp.357–360. Available at: <https://pubs.rsc.org/en/content/articlelanding/2019/cc/c8cc08221a>
30. Chassaing, E., (1983) The kinetics of nickel electrodeposition inhibition by absorbed hydrogen and anions. *Journal of Electroanalytical Chemistry*, 157(1), pp.75–88. Available at: <https://www.sciencedirect.com/science/article/abs/pii/S0022072883803775>
31. Lantelme, F., Seghioer, A. and Derja, A., (1998) Model of nickel electrodeposition from acidic medium. *Journal of Applied Electrochemistry*, 28(907–913(1998)). Available at: <https://link.springer.com/article/10.1023%2FA%3A1003404118601> Accessed 19 January 2021
32. Holm M, O’Keefe T (2000) Evaluation of nickel deposition by electrochemical impedance spectroscopy. *J Appl Electrochem*. <https://doi.org/10.1023/A:1004002303181>
33. Nakano, H., Matsuno, M., Oue, S., Yano, M., Kobayashi, S. and Fukushima, H., (2004) Mechanism of Anomalous Type Electrodeposition of Fe–Ni Alloys from Sulfate Solutions. *MATERIALS TRANSACTIONS*, 45(11), pp.3130–3135. Available at: <https://www.jim.or.jp/journal/epdf3/45/11/3130.pdf> Accessed 4 November 2020
34. Frey, A., Wozniak, N., Nagi, T., Keller, M., Lunderberg, J., Peaslee, G., DeYoung, P. and Hampton, J., (2011) Analysis of Electrodeposited Nickel–Iron Alloy Film Composition Using Particle-Induced X-Ray Emission. *International Journal of Electrochemistry*, 2011, pp.1–7. Available at: <https://www.hindawi.com/journals/ijelc/2011/604395/> Accessed 5 January 2021
35. Plevová M, Hnát J, Bouzek K (2021) Electrocatalysts for the oxygen evolution reaction in alkaline and neutral media. A comparative review. *J Power Sour* 507:230072
36. Ferreira E, Jerkiewicz G (2021) On the electrochemical reduction of β -Ni(OH)₂ to metallic nickel. *Electrocatalysis*. <https://doi.org/10.1007/s12678-021-00643-0>
37. Lyons M, Floquet S (2011) Mechanism of oxygen reactions at porous oxide electrodes. Part 2—Oxygen evolution at RuO₂, IrO₂ and IrxRu1–xO₂ electrodes in aqueous acid and alkaline solution. *Phys Chem Chem Phys* 13(12):5314–5335
38. Meng, X. and Deng, D., (2016) Bio-inspired synthesis of α -Ni(OH)₂ nanobristles on various substrates and their applications. *Journal of Materials Chemistry A*, 4(18), pp.6919–6925. Available at: <https://pubs.rsc.org/en/content/articlelanding/2016/ta/c5ta09329e>
39. Bediako D, Lassalle-Kaiser B, Surendranath Y, Yano J, Yachandra V, Nocera D (2012) Structure-activity correlations in a Nickel–Borate Oxygen evolution catalyst. *J Am Chem Soc* 134(15):6801–6809
40. Klaus S, Cai Y, Louie M, Trotochaud L, Bell A (2015) Effects of Fe electrolyte impurities on Ni(OH)₂/NiOOH Structure and Oxygen Evolution Activity. *The Journal of Physical Chemistry C* 119(13):7243–7254

41. Anantharaj, S., Kundu, S. and Noda, S., (2021) “The Fe Effect”: A review unveiling the critical roles of Fe in enhancing OER activity of Ni and Co based catalysts. *Nano Energy*, 80, p.105514. Available at: <<https://www.sciencedirect.com/science/article/pii/S2211285520310880>>
42. Spanos I, Masa J, Zeradjanin A, Schlögl R (2020) The effect of Iron impurities on transition metal catalysts for the oxygen evolution reaction in alkaline environment: activity mediators or active sites? *Catal Lett* 151(7):1843–1856
43. Hu, H., Tan, M. and Liu, L., (2017) Anomalous codeposition mechanism of Co-Ni alloy nanowires. *Journal of Alloys and Compounds*, 715, pp.384–389. Available at: <<https://www.sciencedirect.com/science/article/pii/S0925838817315499#:~:text=Anomalous%20codeposition%20of%20alloy%20is,deposit%20than%20in%20the%20bath.>>>
44. Li, N., Bediako, D., Hadt, R., Hayes, D., Kempa, T., von Cube, F., Bell, D., Chen, L. and Nocera, D., (2017) Influence of iron doping on tetravalent nickel content in catalytic oxygen evolving films. *Proceedings of the National Academy of Sciences*, 114(7), pp.1486–1491. Available at: <<https://www.pnas.org/content/114/7/1486>>

Publisher's Note Springer Nature remains neutral with regard to jurisdictional claims in published maps and institutional affiliations.

Authors and Affiliations

Yifu Wang¹ · Nigel Williamson² · Richard Dawson^{1,3} · Nuno Bimbo^{1,4} 

✉ Nuno Bimbo
N.Bimbo@soton.ac.uk

¹ Department of Engineering, Lancaster University,
Lancaster LA1 4YW, UK

² Clean Power Hydrogen Group Limited, Doncaster DN2 4BL,
UK

³ LiNa Energy Ltd, Lancaster LA1 4XQ, UK

⁴ School of Chemistry, University of Southampton, Highfield
Campus, Southampton SO17 1BJ, UK